

Postseismic Coulomb stress changes on intra-continental dip-slip faults due to viscoelastic relaxation in the lower crust and lithospheric mantle: insights from 3D finite-element modelling

Meike Bagge^{1,2} · Andrea Hampel¹

Received: 1 August 2016 / Accepted: 20 February 2017 / Published online: 28 March 2017
© Springer-Verlag Berlin Heidelberg 2017

Abstract Earthquakes in the brittle upper crust induce viscoelastic flow in the lower crust and lithospheric mantle, which can persist for decades and lead to significant Coulomb stress changes on receiver faults located in the surrounding of the source fault. As most previous studies calculated the Coulomb stress changes for a specific earthquake in nature, a general investigation of postseismic Coulomb stress changes independent of local geological conditions is still lacking for intra-continental dip-slip faults. Here we use finite-element models with normal and thrust fault arrays, respectively, to show that postseismic viscoelastic flow considerably modifies the original coseismic Coulomb stress patterns through space and time. Depending on the position of the receiver fault relative to the source fault, areas with negative coseismic stress changes may exhibit positive postseismic stress changes and vice versa. The lower the viscosity of the lower crust or lithospheric mantle, the more pronounced are the transient stress changes in the 1st years, with the lowest viscosity having the largest effect on the stress changes. The evolution of postseismic Coulomb stress changes is further controlled by the superposition of transient stress changes caused by viscoelastic relaxation (leading to stress increase or decrease) and the interseismic strain accumulation

(leading to a stress increase). Stress changes induced by viscoelastic relaxation can outweigh the interseismic stress increase such that negative Coulomb stress changes can persist for decades. On some faults, postseismic relaxation and interseismic strain accumulation can act in concert to enhance already positive Coulomb stress changes.

Keywords Postseismic Coulomb stress changes · Viscoelastic relaxation · Numerical modelling · Normal fault · Thrust fault

Introduction

The calculation of Coulomb stress changes after a major earthquake has become an important tool to evaluate the future seismic hazard of a region. In general, positive Coulomb stress changes bring receiver faults closer to failure, while a negative value indicates a delay of the next earthquake (Stein 1999). Coulomb stress changes can arise from a variety of processes during and after the earthquake (e.g. Freed 2005). As a consequence of the coseismic slip on the source fault, receiver faults may experience positive or negative static Coulomb stress changes, depending on the position relative to the source fault (King et al. 1994; Nostro et al. 1997; Lin et al. 2011; Bagge and Hampel 2016). On the other hand, Coulomb stress changes can also be caused by seismic waves (Belardinelli et al. 1999; Pollitz et al. 2012), postseismic fluid flow (Cocco and Rice 2002; Miller et al. 2004; Piombo et al. 2005) and postseismic viscoelastic relaxation (Freed and Lin 1998; Gourmelen and Amelung 2005; Nostro et al. 2001; Pollitz 1997). Postseismic relaxation is the transient response of the viscoelastic layers in the lithosphere to the sudden coseismic slip in the brittle upper crust and acts on timescales of months to

Electronic supplementary material The online version of this article (doi:10.1007/s00531-017-1467-8) contains supplementary material, which is available to authorized users.

✉ Meike Bagge
bagge@gfz-potsdam.de

¹ Institut für Geologie, Leibniz Universität Hannover, Callinstraße 30, 30167 Hanover, Germany

² Present Address: Deutsches GeoForschungsZentrum GFZ, Telegrafenberg, 14473 Potsdam, Germany

decades, depending on the viscosity of the excited layers (e.g. Nur and Mavko 1974). In the early postseismic phase, the effect of viscoelastic relaxation on displacements and Coulomb stress changes may be intermingled with afterslip but the effect of the local afterslip rapidly decreases, while the importance of viscoelastic relaxation—which acts on a larger regional scale—relative to afterslip increases (Diao et al. 2014; Hampel and Hetzel 2015; Lambert and Barbot 2016). Modelling and geodetic data of the 2011 $M_w=9.0$ Tohoku–Oki earthquake (Japan) showed that viscoelastic relaxation plays a dominant role over afterslip even during short-term postseismic deformation (Sun et al. 2014).

While there is a large number of studies on coseismic Coulomb stress changes (e.g. King et al. 1994; Lin and Stein 2004; Nostro et al. 1997; Parsons et al. 2008), stress changes due to postseismic viscoelastic relaxation have less often been quantified, and mostly for strike-slip faults (e.g. Freed and Lin 2001; Hearn et al. 2002; Masterlark and Wang 2002; Smith and Sandwell 2006). Fewer studies were dedicated to the postseismic stress interaction between normal faults or thrust faults (e.g. Freed and Lin 1998; Nalbant and McCloskey 2011; Nostro et al. 2001; Wang et al. 2014). Interactions between normal faults due to postseismic relaxation have been investigated by Nostro et al. (2001). Using self-gravitating and stratified spherical Earth models with viscoelastic layers, they calculated co- and postseismic stress changes on timescales up to centuries and on spatial scales up to a few hundreds of kilometres to evaluate the influence of the rheological stratification and the thickness of the layers. They compared their models with the normal faults in the Apennines (Italy) and concluded that the relaxation tends to increase the Coulomb stresses. Freed and Lin (1998) investigated—based on a potential connection between the 1971 San Fernando and 1994 Northridge thrust fault earthquakes—the time-dependent stress changes caused by relaxation in the viscous lower crust and upper mantle using two-dimensional finite-element models. Their results indicate that postseismic creep generates a stress triggering zone at the base of the upper crust. Finally, several studies have computed postseismic Coulomb stress changes after the 2008 Wenchuan (China) oblique thrust fault earthquake (Chen et al. 2011; Luo and Liu 2010; Nalbant and McCloskey 2011; Wang et al. 2014). Using a finite-element model that includes an upper crust and a viscoelastic layer representing both lower crust and lithospheric mantle, Luo and Liu (2010) studied the effects of the 2008 earthquake resolved on the major faults of south-eastern Tibet. On a larger scale, Chen et al. (2011) used a finite-element block model to calculate the Coulomb stress changes on major strike-slip and thrust fault for the entire Tibetan Plateau; however, for all thrust faults (except the Beichuan thrust) a vertical dip was assumed. Nalbant and McCloskey (2011) focused on the region around the 2008

earthquake and included previous earthquakes as well as a rheologically stratified lithosphere. All analyses reached a similar general conclusion that positive stress changes can be expected for the region south-west and north-east of the location of the 2008 event. Indeed, in April 2013, a M6.6 thrust earthquake occurred south-west of the fault ruptured during the 2008 event (Wang et al. 2014), i.e. in the region, where positive Coulomb stress changes had been predicted for thrust faults (Chen et al. 2011; Luo and Liu 2010; Nalbant and McCloskey 2011; Parsons et al. 2008; Wang et al. 2014).

In contrast to previous studies, which were mostly dedicated to a specific setting or earthquake, the scope of our study is a better understanding of the general patterns of postseismic Coulomb stress changes on normal and thrust faults. Our study is a follow-up investigation of our previous analysis of coseismic Coulomb stress changes (Bagge and Hampel 2016) and uses the same set-up with arrays of 11 normal or thrust faults. Based on the same coseismic stress changes, we analyse the spatiotemporal evolution of postseismic Coulomb stress changes on individual fault planes caused by viscoelastic relaxation in space and time. In different experiments, we varied the viscosities of the lower crust and lithospheric mantle. Our analysis includes an evaluation of the differences between the two types of faults as well as the relative importance between stress changes arising from viscoelastic relaxation and stress changes caused by ongoing extension or shortening. In a second step, we link the Coulomb stress changes to the postseismic movements in the crust and lithospheric mantle to explain the obtained stress change distributions.

Model set-up

For our parameter study, we used the commercial finite-element software ABAQUS (version 6.14) to create three-dimensional models with normal and thrust fault arrays, respectively (cf., Bagge and Hampel 2016). Each model represents a 200×200 km wide and 100-km-thick continental lithosphere, which consists of an elastic upper crust, a viscoelastic lower crust and a viscoelastic lithospheric mantle (Fig. 1). The thickness and rheological parameters of the layers (density ρ , Poisson's ratio ν , Young's modulus E and viscosity η) are shown in Fig. 1. Viscoelastic behaviour is implemented as linear, temperature-independent Maxwell viscoelasticity. Although this rheology represents a simplification of the actually depth-dependent and possibly nonlinear viscoelastic behaviour of the lower crust and lithospheric mantle (e.g. Ellis et al. 2006; Freed and Bürgmann 2004), the implementation of viscoelastic layers itself is an advantage compared to the commonly used homogeneous elastic halfspace models based on Okada (1992). Furthermore, linear viscosities have been derived

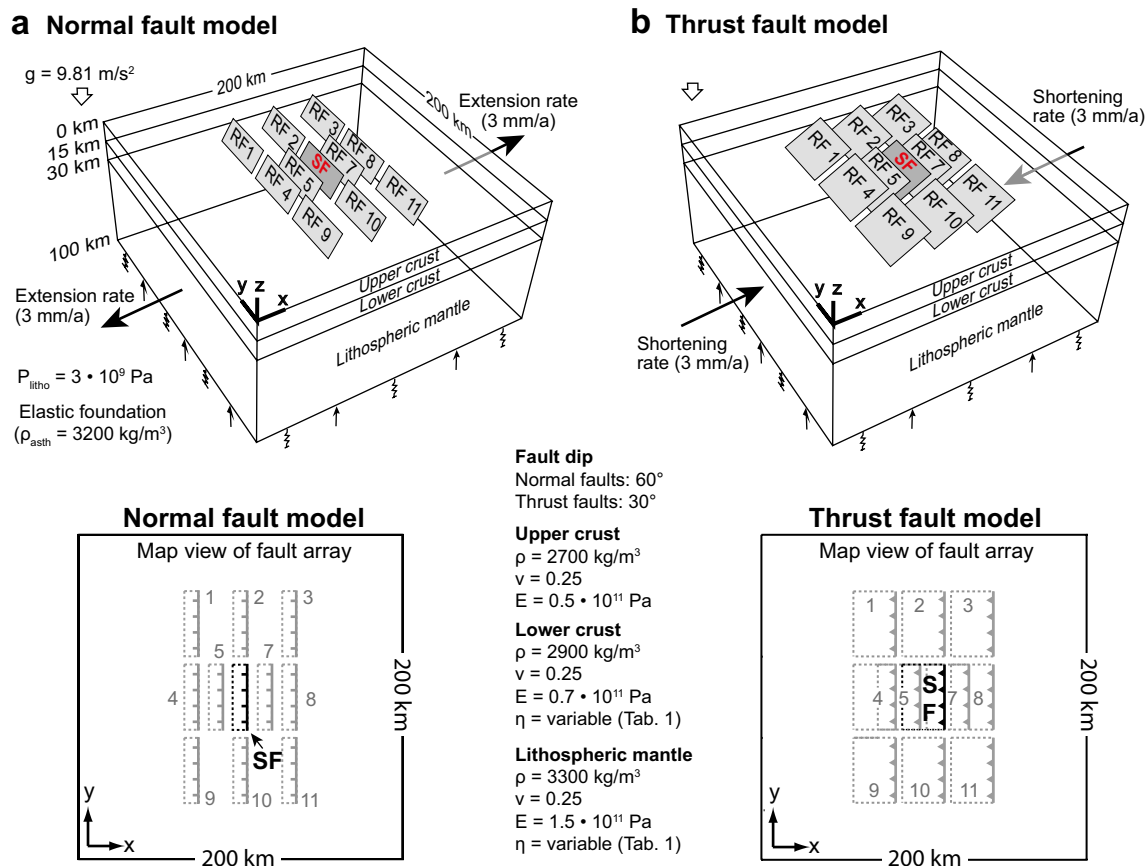


Fig. 1 Perspective view of the three-dimensional models with arrays of 40-km-long (a) normal faults and (b) thrust faults. A source fault (SF) and ten receiver faults (RF) are embedded in the upper crust. Faults are centred in the upper crust (see map view of model surface). A velocity boundary condition is applied to the model sides in the yz -

plane to extend or shorten the model at a total rate of 6 mm/a, which initiates slip on the faults. Abbreviations are ρ density, E Young's modulus, ν Poisson's ratio, η viscosity, g acceleration due to gravity, P_{litho} lithostatic pressure and ρ_{asth} density of the asthenosphere

by a number of inversion studies, ranging from reservoir loading (e.g. Kaufmann and Amelung 2000) to postseismic deformation patterns (e.g. Nishimura and Thatcher 2003; Gourmelen and Amelung 2005).

In the model centre, a source fault (called SF in Fig. 1) that will experience the coseismic slip during the analysis, and ten surrounding receiver faults are embedded in the upper crust. The 60° -dipping normal faults (Fig. 1a) and 30° -dipping thrust faults (Fig. 1b) are 40 km long and extend from the model surface to the bottom of the upper crust. Following natural spatial configurations of faults, for example, in the Basin and Range Province (Haller et al. 2004), the Aegean region (Roberts and Michetti 2004) and the foreland of the Tibetan (Meyer et al. 1998; Hetzel et al. 2004), we apply distances between the faults of ≥ 15 km in the x -direction and ≥ 5 km in the y -direction. The locations of the receiver faults around the source fault are chosen such that the postseismic Coulomb stress changes in the surrounding of the source fault can be probed

systematically: four receiver faults are located in the footwall and hanging wall of the source fault (RF4, 5, 6, 7), two faults are located along-strike of the source fault's tips (RF2, 10), and four other faults are located outside of the immediate hanging wall and footwall of the source fault (RF1, 3, 9, 11). Compared to studies of Coulomb stress changes that resolve the stress change at arbitrary points or planes (e.g. Nostro et al. 2001), our approach has the advantage that the finite extent of the fault plane as well as the slip accumulation before the earthquake cycle is taken into account. Gravity is implemented as a body force. Isostatic effects are simulated by a lithostatic pressure of 3×10^9 Pa and an elastic foundation, which are both applied to the model bottom (depicted in Fig. 1 as arrows and springs, respectively). The stiffness of the foundation is calculated from the product of density of the asthenosphere and gravitational acceleration. The model sides in the xz -plane are fixed in the y -direction. Model sides and bottom are free to move in the vertical direction. The yz -plane is controlled

by a velocity boundary condition in the x -direction. All models are meshed by linear tetrahedral elements with an edge length of 1 km near the faults, which increases to 3 km at the model margins.

Each model run consists of a series of quasi-static analysis steps. After reaching a state of isostatic equilibrium, the model is extended or shortened at a total rate of 6 mm/a in the x -direction (Fig. 1a, b) throughout the remaining model time, which generates the tectonic background deformation and initiates slip on the faults. Slip initiation is controlled by the Mohr–Coulomb criterion $|\tau_{\max}| = c + \mu\sigma_n$, where τ_{\max} is the critical shear stress, c is the cohesion (zero in our model), σ_n is the normal stress and μ is the coefficient of friction (0.6 in our model). During the initial model phase, all faults slip continuously to let them achieve a constant slip rate (cf., Hampel and Hetzel 2012). After all faults have attained a constant slip rate, the earthquake cycle is simulated in three steps (cf., Hampel and Hetzel 2015; Hampel et al. 2013). In the pre-seismic phase, all faults are locked. In the coseismic phase, we unlock only the source fault (SF in Fig. 1), which leads to sudden slip (= model earthquake). Note that the slip distribution is not prescribed but develops self-consistently in accordance with the strain accumulated during the pre-seismic phase. In the models of this study, we define the duration of the pre-seismic phase such that the maximum coseismic slip is 2 m on the 40-km-long fault during the coseismic phase. The equivalent moment magnitude calculated from the seismic moment is 6.8 and 6.9 in the normal and thrust fault model, respectively. All receiver faults remain locked during the coseismic phase. In the post-seismic phase, we lock all faults again. Note that no afterslip occurs on the source fault during the post-seismic phase, as the fault fully relaxes during the coseismic phase (Ellis et al. 2006). Extension/shortening of the model continues during the post-seismic phase, leading to average values of 0.01–0.02 MPa for the interseismic stress increase on the fault planes.

Figure 2 shows the coseismic displacement and stress fields, the coseismic slip distribution and the resulting static Coulomb stress changes as derived from the normal and thrust fault models with a viscosity of 10^{20} and 10^{23} Pa s for the lower crust and lithospheric mantle, respectively (Bagge and Hampel 2016). Note that the coseismic displacements and stress changes do not depend on the viscosity structures and are hence the same in all models of this study. They provide the common basis for our analysis of the post-seismic Coulomb stress changes, for which we varied the viscosities of the lower crust and lithospheric mantle in different experiments (Table 1). The coseismic displacements—plotted with their magnitude and direction along a cross section through the central part of the model—show the typical footwall uplift

and hanging wall subsidence in the normal fault model and hanging wall uplift and footwall subsidence in the thrust fault model (Fig. 2a). On the source fault SF, the coseismic slip reaches its maximum in the centre of the fault's surface trace and has an elliptical distribution (Fig. 2b). The coseismic displacements in the elastic upper crust lead to coseismic loading of the viscoelastic lower crust, with the maximum coseismic stress increase being located around the lower fault tip in the upper part of the lower crust (Fig. 2c). This coseismic stress increase in the lower crust provides the initial condition for the subsequent viscoelastic relaxation in our models, i.e. it is this stress that is dissipated by viscous creep during the post-seismic model phase. Note that this stress increase at the lower fault tip is consistent with other numerical models on coseismic loading of the lower crust (e.g. Ellis and Stöckhert 2004; Ellis et al. 2006; Nüchter and Ellis 2010, 2011) although—in contrast to these studies—the coseismic slip on our source fault does not actually reach into the lower crust. Geodetic inversion models showed that coseismic slip penetrated into the brittle-viscous transition zone during some earthquakes (e.g. Rolandone et al. 2004), although this is not always the case (e.g. Ryder et al. 2012; Serpelloni et al. 2012).

The coseismic Coulomb stress changes on our model fault planes are shown in Fig. 2d. We calculated the Coulomb stress change ΔCFS by $\Delta\text{CFS} = \Delta\tau - \mu'\Delta\sigma_n$, where $\Delta\tau$ is the change in shear stress (positive in direction of source fault slip), μ' is the effective coefficient of friction, and $\Delta\sigma_n$ is the change in normal stress (positive if fault is clamped) (e.g. Freed 2005; Stein et al. 1992; Stein 1999, 2003). A positive stress change implies that slip is promoted on the receiver faults in the direction of the slip of the source fault and the direction given by the regional stress field. In contrast, a negative Coulomb stress change means that slip on the fault in direction of the slip on the source fault is hampered. The earthquake in our model with 2 m of coseismic slip leads to static Coulomb stress changes on the receiver faults, which range from a few bar to several MPa depending on the distance to the source fault (Fig. 2d). Both positive and negative Coulomb stress changes are observed, with changes in the sign occurring both along strike of individual receiver fault as well as in their down-dip direction (Bagge and Hampel 2016). Generally, faults located in the hanging wall and footwall of the source fault (RF4–8) experience primarily negative coseismic stress changes with a symmetric distribution on each fault plane. Receiver faults RF5 and 7 located close to the source fault show significant positive stress changes in some parts of their fault plane. Faults RF2 and 10 positioned in the along-strike prolongation of the source fault undergo exclusively positive Coulomb stress changes and exhibit an asymmetric Coulomb stress change

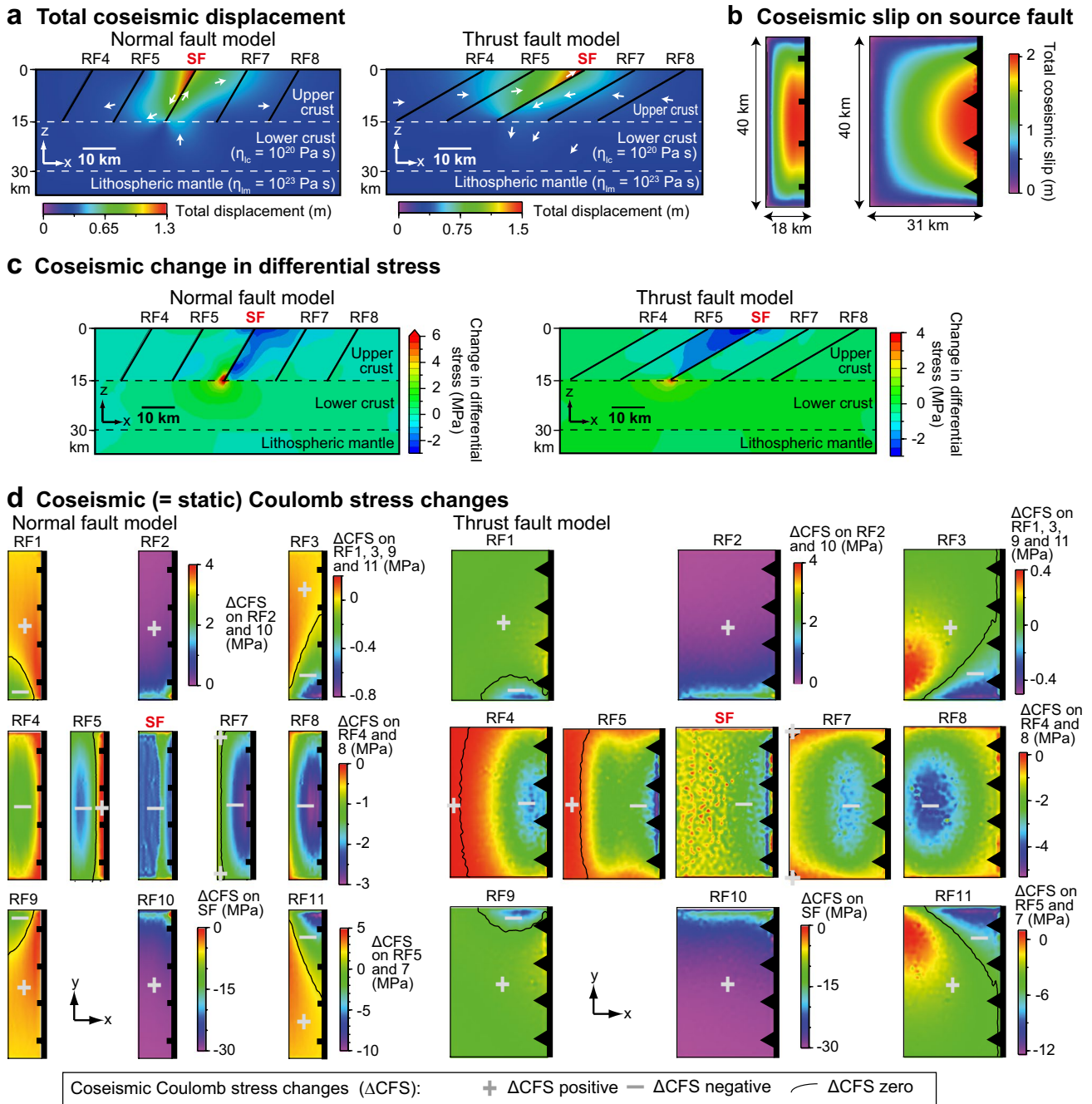


Fig. 2 Coseismic displacements, fault slip, stress fields and resulting coseismic Coulomb stress changes (modified from Bagge and Hampel (2016)). **a** Cross sections through the central part of the model showing the total coseismic displacement field. **b** Coseismic slip distribution on the normal and thrust source faults. Maximum

slip is 2 m. **c** Cross sections through the central part of the model showing the coseismic change in the differential stress. **d** Coseismic Coulomb stress changes caused by a model earthquake on the source fault. See text for details

distribution. Receiver faults RF1, 3, 9 and 11 also show an asymmetric stress change distribution, with mostly positive stress changes but also high values of negative stress changes (Fig. 2d). Note that the distribution of Coulomb stress changes on RF1, 2 and 3 are mirror images to RF9, 10 and 11.

Model results

We ran experiments with different viscosities of the lower crust and lithospheric mantle (Table 1). The viscosity structure in our models reflects the two endmember possibilities for the rheological layering of the lithosphere

Table 1 Viscosities of the lower crust and lithospheric mantle in the models used for this study

Model name	Fault type	Viscosity of lower crust η_{lc} (Pa s)	Viscosity of lithospheric mantle η_{lm} (Pa s)	Viscosity structure
NP1	Normal	10^{20}	10^{23}	$\eta_{lc} < \eta_{lm}$
TP1	Thrust			
NP2	Normal	10^{18}	10^{22}	
TP2	Thrust			
NP3	Normal	10^{18}	10^{23}	
TP3	Thrust			
NP4	Normal	10^{21}	10^{19}	$\eta_{lc} > \eta_{lm}$
TP4	Thrust			
NP5	Normal	10^{22}	10^{19}	
TP5	Thrust			
NP6	Normal	10^{22}	10^{21}	
TP6	Thrust			

(e.g. Burov and Watts 2006): in the first three models (NP/TP1-3), the lithosphere has a weak lower crust and a strong lithospheric mantle, whereas the other three models have a strong lower crust and a weak lithospheric mantle. The first viscosity structure is found, for example, beneath the Himalaya–Tibet system, as indicated by geophysical data (Chen and Molnar 1983; Klempner 2006), inversion of lake shoreline deflection (Shi et al. 2015) and postseismic lower crustal flow (Ryder et al. 2014). In contrast, the presence of a strong lower crust and a weak lithospheric mantle has been reported, for example, from the actively extending Basin and Range Province based on postglacial rebound patterns (Bills et al. 1994), postseismic deformation (Amelung and Bell 2003; Gourmelen and Amelung 2005; Nishimura and Thatcher 2003) and deformation caused by reservoir loading (Kaufmann and Amelung 2000). As the viscosity structure of the lithosphere remains debated (e.g. Bürgmann and Dresen 2008; Jackson 2002), we computed the normal and thrust fault models for all viscosity structures (Table 1).

For the evaluation of our results, we first show the postseismic Coulomb stress changes on the fault planes at the same timepoints (1st, 10th and 20th year after the earthquake) to allow a direct comparison between the models, regardless of the characteristic timescales of the applied viscosities. We chose the 1st year after the earthquake to show that viscoelastic relaxation considerably modifies the coseismic Coulomb stress changes already during the early postseismic phase (Figs. 3, 4; Online Resource Figs. S1, S2). We further show the results at the 10th and 20th years to illustrate that the postseismic Coulomb stress change patterns caused of viscoelastic relaxation change through time and are still recognizable after 1–2 decades (Figs. 5, 6; Online Resource Figs. S3, S4). In addition to the figures showing the stress changes on the fault planes, Figs. 7 and 8 show the temporal evolution of the postseismic Coulomb

stress along profiles across the fault planes and at the centres of selected receiver faults.

Postseismic Coulomb stress changes in the 1st year after the earthquake

In the 1st year after the earthquake, the original distribution of the coseismic Coulomb stress changes undergoes considerable modifications on most receiver faults (Figs. 3, 4). Depending on the viscosity structure of the lithosphere and the position of the receiver fault relative to the source fault, the sign of the Coulomb stress changes can be reversed on some faults. For example, receiver fault RF7 was characterized by mainly negative coseismic stress changes but shows mainly positive stress changes during the first postseismic year in both thrust and normal fault models. A common characteristic of both coseismic and postseismic stress changes is that the stress change distribution is symmetric on faults RF4-8 but asymmetric on faults RF1-3 and 9-11. The order of magnitude of the postseismic Coulomb stress changes on the receiver faults ranges between 0.01 and 2.5 MPa. Postseismic Coulomb stress changes on the source fault are generally an order of magnitude higher than on the receiver faults and have a positive sign in all models. In the following, we will describe the Coulomb stress changes resulting from the different viscosity structures of the model lithosphere in more detail.

In the normal (NP1) and thrust (TP1) models with viscosities of 10^{20} and 10^{23} Pa s for the lower crust and lithospheric mantle, respectively, all faults, except RF5, experience positive stress changes (Figs. 3a, 4a). Faults RF1-3 and 9-11 exhibit a homogeneous Coulomb stress distribution with an average stress increase of 0.02 MPa. In contrast, faults in the hanging wall and footwall of the source fault (RF4, 7 and 8) show a gradient in the positive stress changes. On RF4, the magnitude of the positive stress

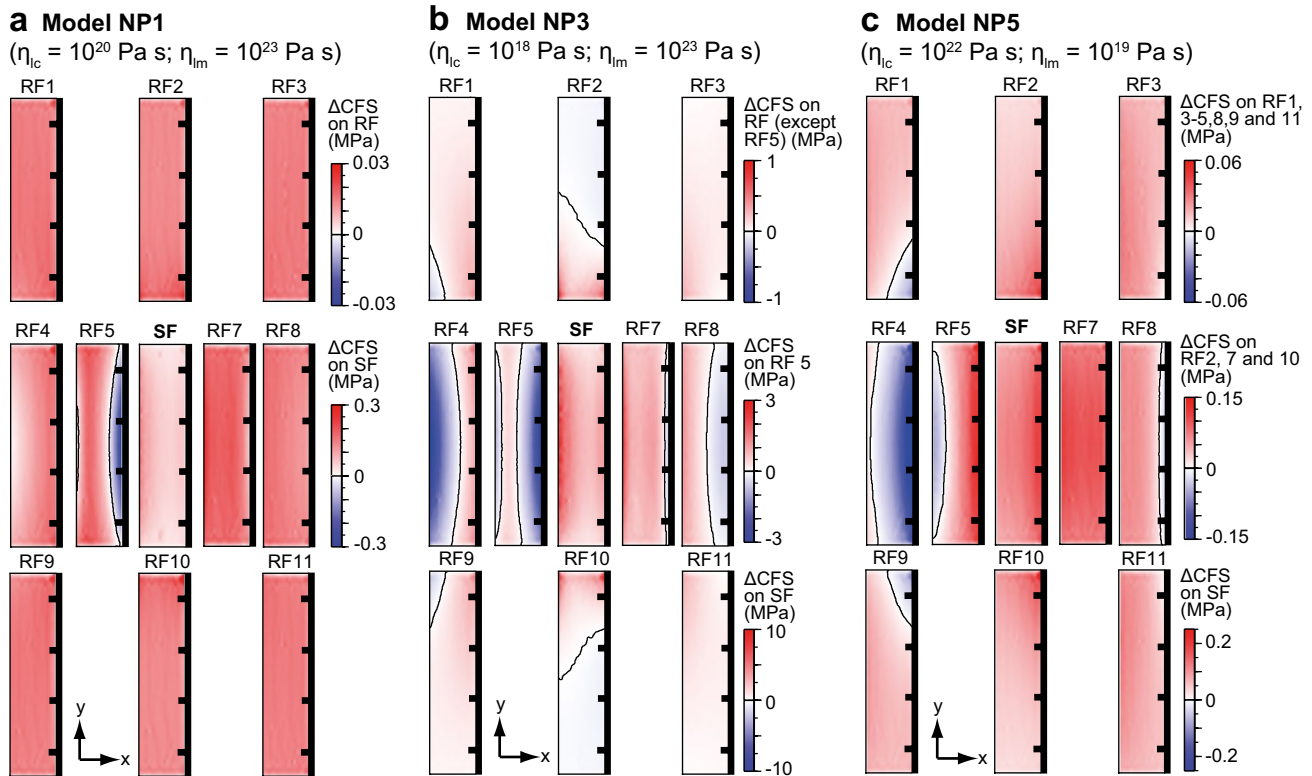
Normal fault models: Postseismic Coulomb stress changes during the first year after the earthquake

Fig. 3 Postseismic Coulomb stress changes (ΔCFS) on receiver faults (RF) in the 1st year after the earthquake on the source fault (SF) as derived from normal fault model (a) NP1 ($\eta_{lc}=10^{20}$ Pa s; $\eta_{lm}=10^{23}$ Pa s), (b) NP3 ($\eta_{lc}=10^{18}$ Pa s; η_{lm} of 10^{23} Pa s) and (c) NP5 ($\eta_{lc}=10^{22}$ Pa s; $\eta_{lm}=10^{19}$ Pa s). For results from models NP2, NP4 and NP6 see in Online Resource Figure S1. Note that the dis-

tance between the faults is not to scale. The distance in the x -direction between the fault surface traces is 15 km in the centre row (RF4–8) and 30 km in the upper (RF1–3) and lower (RF9–11) rows of the fault array. The distance in the y -direction is 5 km. Areas with positive Coulomb stress changes (red) and negative stress changes (blue) are separated by a black line where $\Delta\text{CFS}=0$

change increases towards the surface, whereas on RF7 and 8 the Coulomb stress change increases towards the down-dip edge of the fault. The highest stress increase occurs in the lower part of RF7 in the normal fault model (0.03 MPa) and in the upper part of RF5 in the thrust fault model (0.05 MPa). In contrast to the other ten faults, receiver fault RF5 also shows negative stress changes, which occur in two separate areas on the fault plane. In the normal fault model, the highest stress decrease (-0.018 MPa) occurs in a large stress shadow zone in the upper part of the fault; in its lower part, a second, smaller stress shadow zone is observed (Fig. 3a). In the thrust fault model, negative stress changes occur in the lower part of the fault, where they reach a value of up to -0.01 MPa, and in the fault centre (Fig. 4a).

Models with a lower crustal viscosity of 10^{18} Pa s but different viscosities of the lithospheric mantle (NP2/3, TP2/3) show almost the same pattern and magnitudes of the Coulomb stress changes (Figs. 3b, 4b; Online Resource Figs. S1a, S2a). Compared to models NP1 and

TP1, the Coulomb stress changes are 1–2 orders of magnitude higher, and almost all faults experience both positive and negative stress changes (see Figs. 3, 4). Only the source fault and the normal faults RF3 and 11 show solely positive stress changes. Notably, many areas that experienced a coseismic stress increase show a postseismic stress decrease and *vice versa*. Only faults 1 and 9 show roughly the same distribution of stress triggering and shadow zones as during the coseismic phase. In the normal fault model, the highest values of stress increase occur on receiver fault RF7 (0.79 MPa) and on RF5 (0.55 MPa). Positive stress changes of up to ~ 0.4 MPa are observed on RF4 and 8 as well as in the surface corners of RF1 and 9 (Fig. 3b, S1a). Compared to the normal fault models, positive Coulomb stress changes in the thrust fault models reach much higher values, for example on RF5 (2.19 MPa), RF7 (1.73 MPa) and RF8 (1.49 MPa). On thrust faults RF1–4 and 9–11, maximum values vary between 0.14 and 0.47 MPa. The largest stress decrease occurs on fault RF5, which shows -2.27 MPa in the normal fault models (Fig. 3b, S1a) and

Fig. 4 Postseismic Coulomb stress changes (Δ CFS) on receiver faults (RF) in the 1st year after the earthquake on the source fault (SF) as derived from thrust fault model (a) TP1 ($\eta_{lc} = 10^{20}$ Pa s; $\eta_{lm} = 10^{23}$ Pa s), (b) TP3 ($\eta_{lc} = 10^{18}$ Pa s; $\eta_{lm} = 10^{23}$ Pa s) and (c) TP5 ($\eta_{lc} = 10^{22}$ Pa s; $\eta_{lm} = 10^{19}$ Pa s). For results from models TP2, TP4 and TP6, see Online Resource Figure S2. Note that the distance between the faults is not to scale. The distance in the x -direction between the fault surface traces is 15 km in the centre row (RF4-8) and 30 km in the upper (RF1-3) and lower (RF9-11) rows of the fault array. The distance in the y -direction is 5 km. Areas with positive Coulomb stress changes (red) and negative stress changes (blue) are separated by a black line where Δ CFS = 0

Thrust fault models: Postseismic Coulomb stress changes during the first year after the earthquake

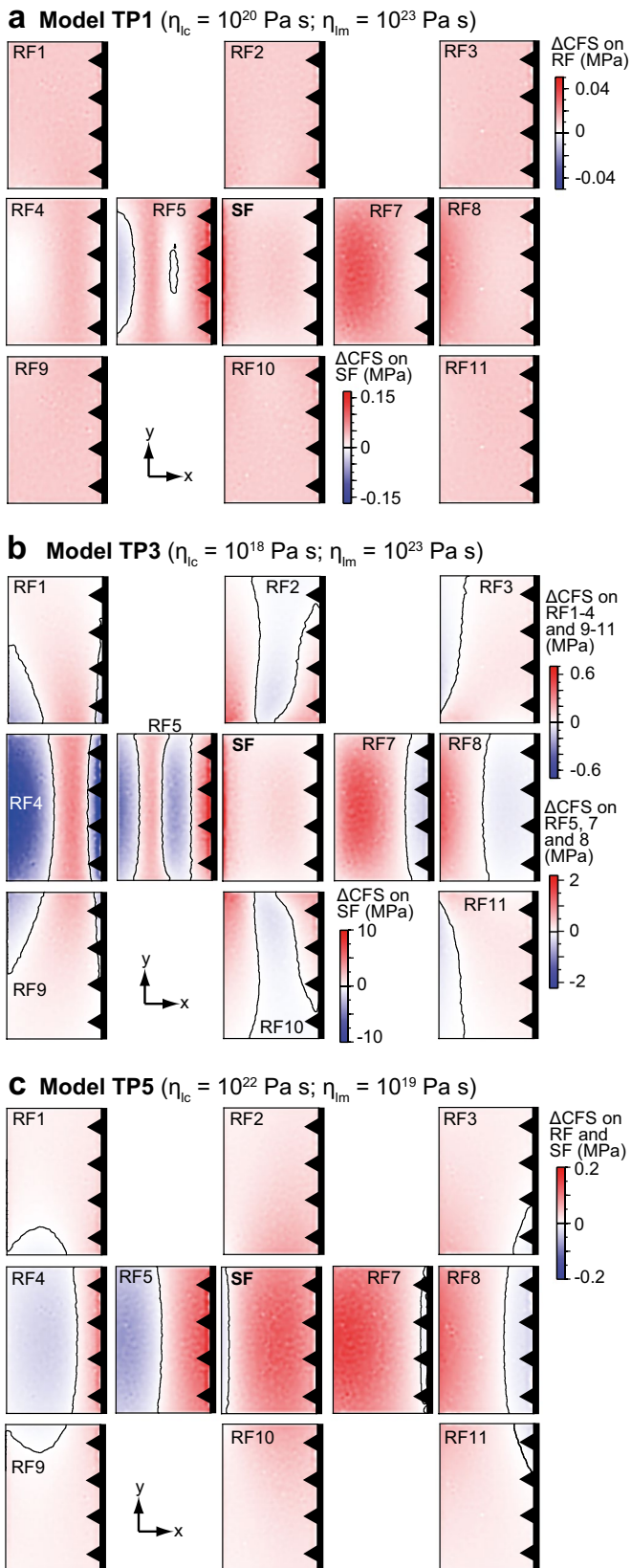
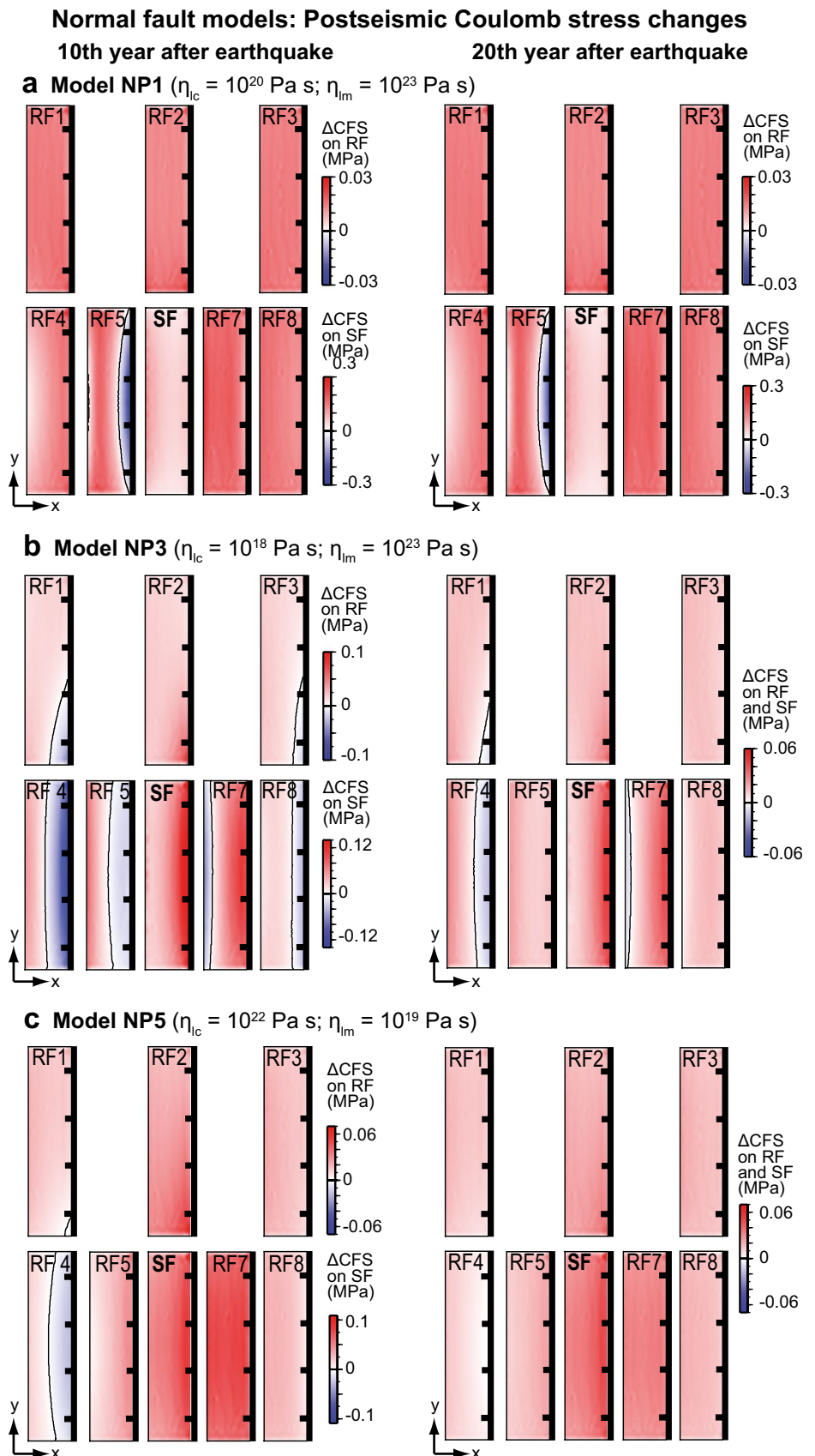


Fig. 5 Postseismic Coulomb stress changes (Δ CFS) on receiver faults (RF) in the 10th and 20th year after the earthquake on the source fault (SF) as derived from normal fault model (a) NP1 ($\eta_{lc} = 10^{20}$ Pa s; $\eta_{lm} = 10^{23}$ Pa s), (b) NP3 ($\eta_{lc} = 10^{18}$ Pa s; $\eta_{lm} = 10^{23}$ Pa s) and (c) NP5 ($\eta_{lc} = 10^{22}$ Pa s; $\eta_{lm} = 10^{19}$ Pa s). For results from models NP2, NP4 and NP6, see Online Resource Figure S3. Note that the distance between the faults is not to scale. The distance in the x -direction between the fault surface traces is 15 km in the centre row (RF4-8) and 30 km in the *upper* (RF1-3) row of the fault array. The distance in the y -direction is 5 km. Areas with positive Coulomb stress changes (*red*) and negative stress changes (*blue*) are separated by a black line where Δ CFS=0. Stress changes on RF9-11 (not shown in figure) are mirror images to the stress changes on RF1-3



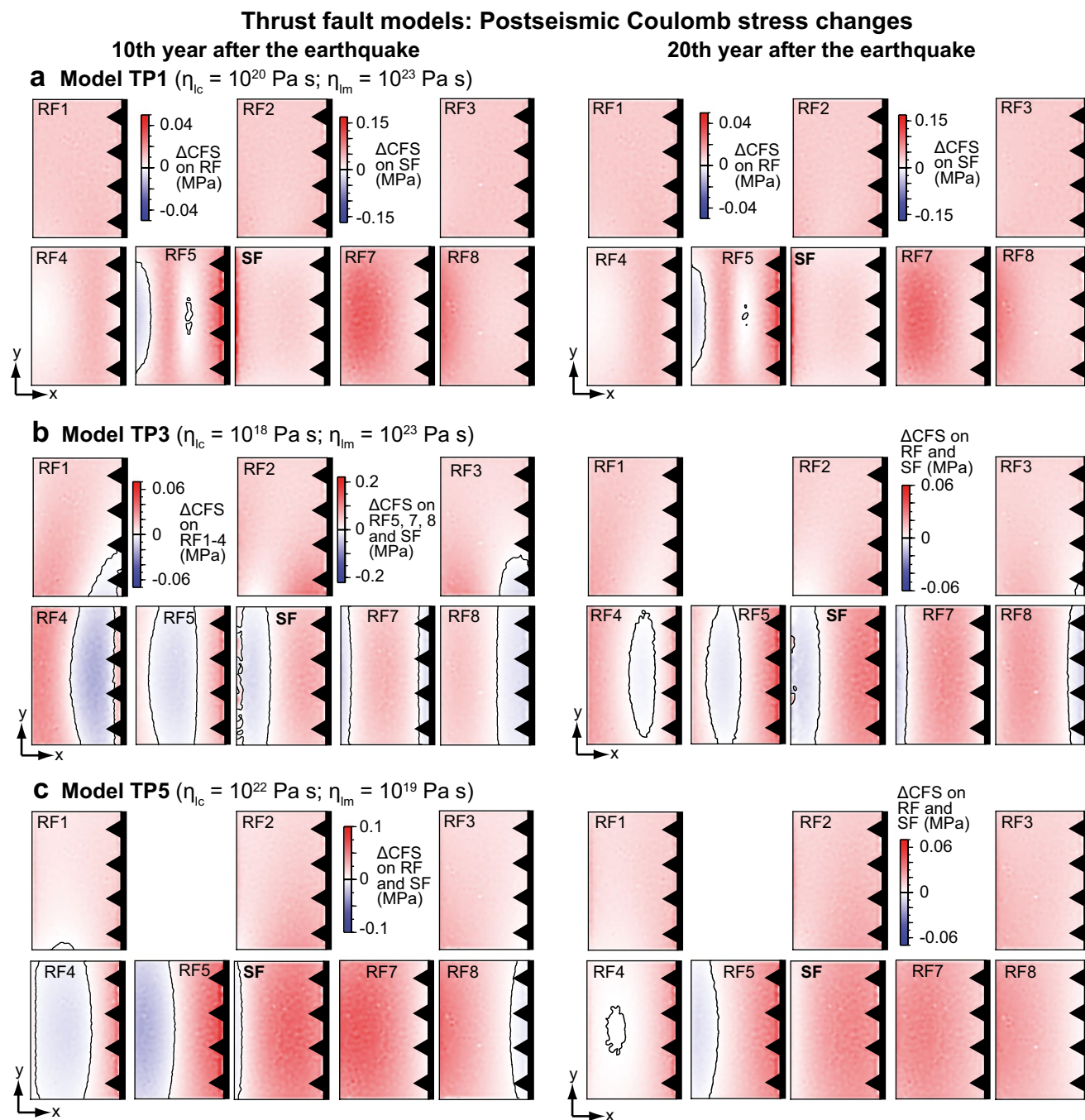


Fig. 6 Postseismic Coulomb stress changes (Δ CFS) on receiver faults (RF) in the 10th and 20th year after the earthquake on the source fault (SF) as derived from thrust fault model (a) TP1 ($\eta_{lc} = 10^{20}$ Pa s; $\eta_{lm} = 10^{23}$ Pa s), (b) TP3 ($\eta_{lc} = 10^{18}$ Pa s; $\eta_{lm} = 10^{23}$ Pa s) and (c) TP5 ($\eta_{lc} = 10^{22}$ Pa s; $\eta_{lm} = 10^{19}$ Pa s). For results from models TP2, TP4 and TP6, see Online Resource Figure S4. Note that the distance between the faults is not to scale. The distance

in the x -direction between the fault surface traces is 15 km in the centre row (RF4–8) and 30 km in the upper (RF1–3) row of the fault array. The distance in the y -direction is 5 km. Areas with positive Coulomb stress changes (*red*) and negative stress changes (*blue*) are separated by a *black line* where Δ CFS=0. Stress changes on RF9–11 (not shown in figure) are mirror images to the stress changes on RF1–3

–1.17 MPa in the thrust fault models (Fig. 4b, S2a). On the normal fault RF5, the maximum value occurs in a broad stress shadow zone that reaches the surface; a smaller zone with negative stress changes is located near the down-dip

edge of the fault. On thrust fault RF5, the highest stress decrease occurs near the down-dip edge of the fault; a second stress shadow zone with almost the same magnitudes is located in the fault centre. Other stress shadow zones

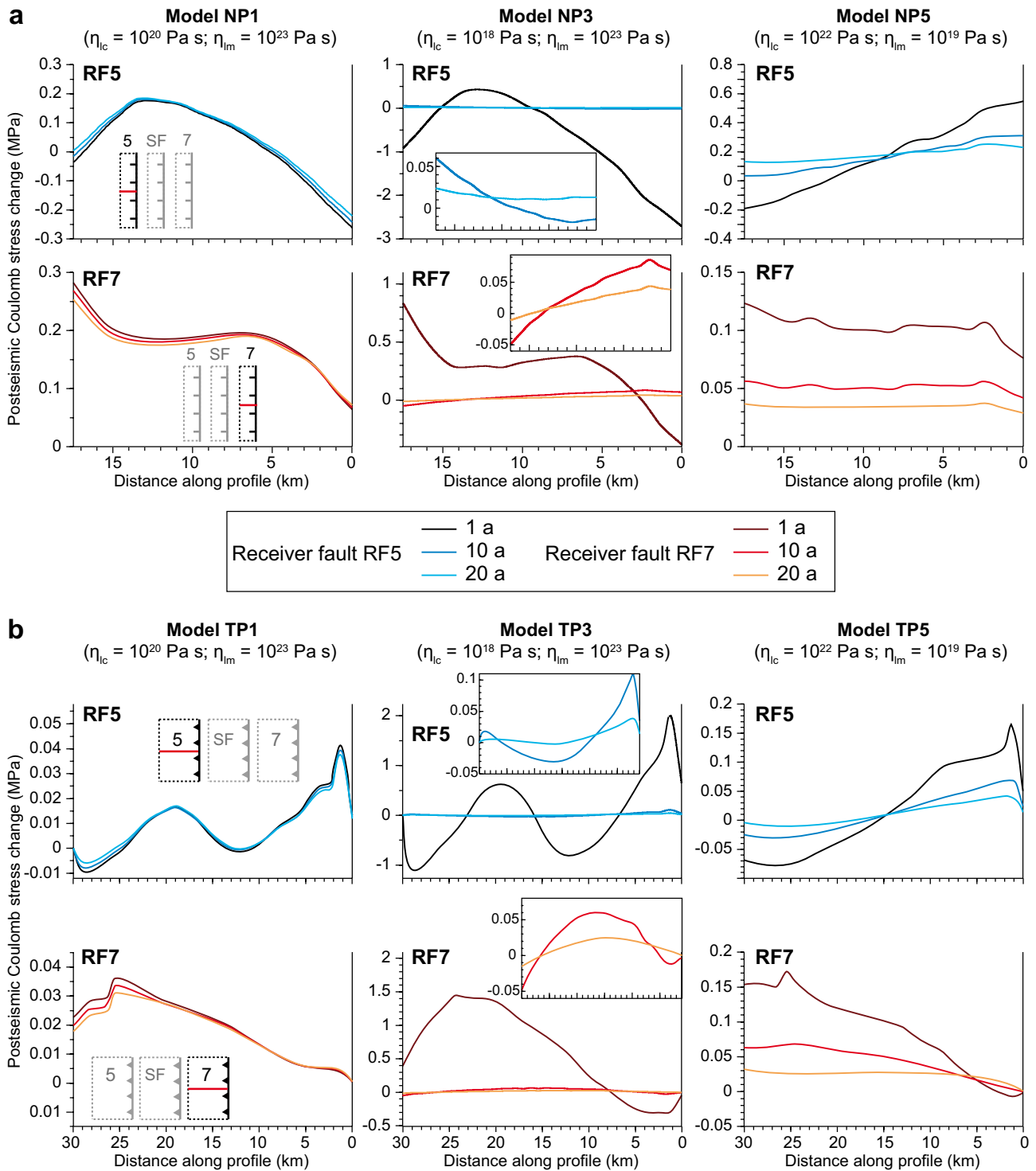


Fig. 7 Profiles showing the postseismic Coulomb stress change in down-dip direction along receiver faults RF5 and 7 in (a) normal fault models NP1, NP3 and NP5 and (b) thrust fault models TP1, TP3 and

TP5. Insets in the central panel show the stress changes in the 10th and 20th year in the models NP3/TP3

occur in the lower parts of normal faults RF4 (−0.97 MPa) and RF1 and 9 (−0.20 MPa), in the upper parts of RF7 and 8 (−0.2 MPa), and in the distal part of RF2 and 10

(−0.87 MPa). In the thrust fault model, two stress shadow zones exist on RF1, 4 and 9, one at the surface area and the other in the lower part of the faults, where maximum values

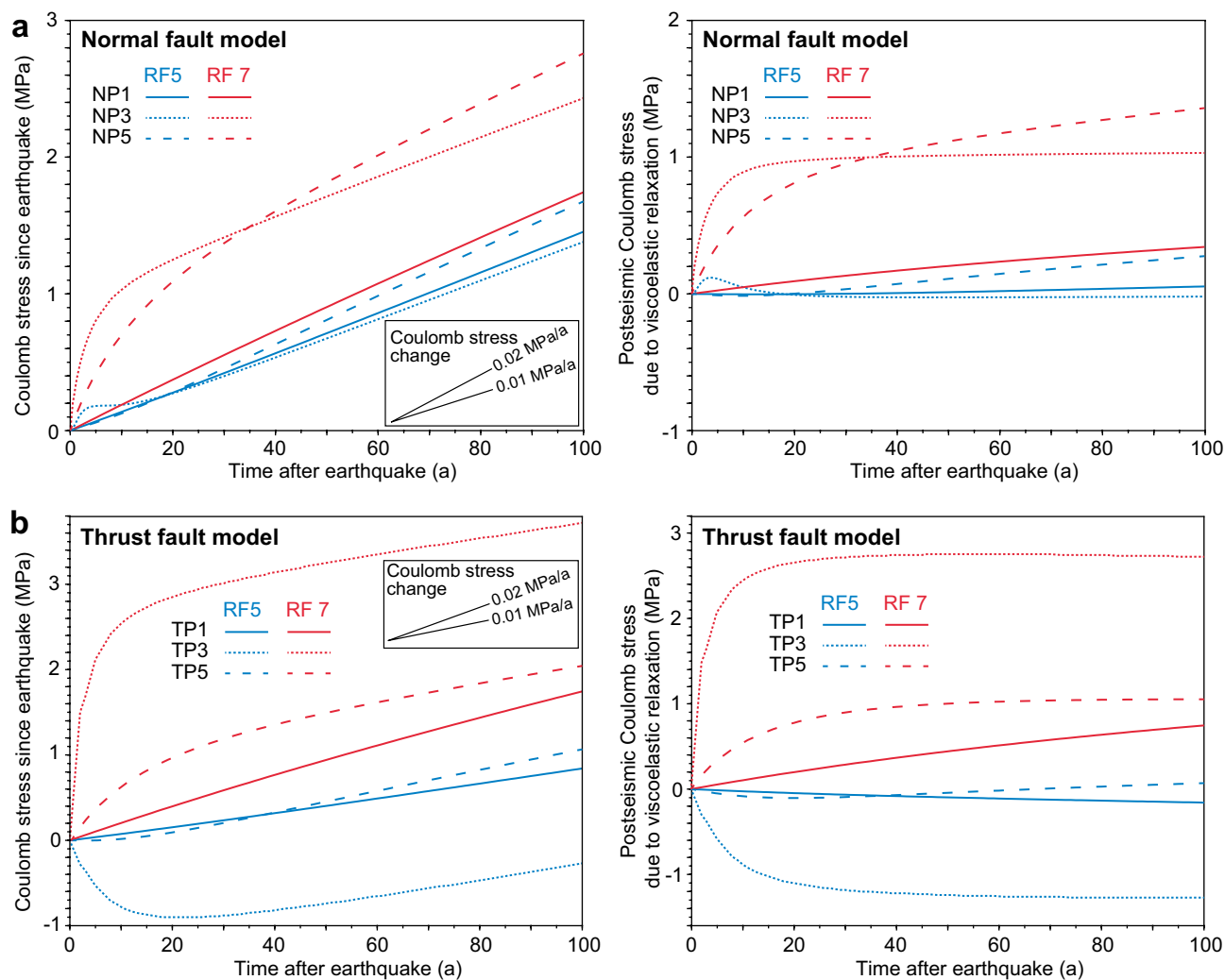


Fig. 8 Temporal evolution of the postseismic Coulomb stress at the centres of faults RF5 and 7 in (a) normal fault models NP1, NP3 and NP5 and (b) thrust fault models TP1, TP3 and TP5. Diagrams in the left column show the total postseismic Coulomb stress due to vis-

coelastic relaxation and interseismic stress increase. Diagrams in the right column show the postseismic Coulomb stress due to viscoelastic relaxation only

of up to -0.69 MPa (RF4) and -0.24 MPa (RF1 and 9) are reached. On thrust faults RF2 and 10, the stress shadow zone runs across the fault centre and is located between two stress triggering zones. In contrast, thrust faults RF7 (-0.47 MPa) and 8 (-0.21 MPa) show a similar stress change distribution as their counterparts in normal fault model, with zones of stress decrease near the surface.

Postseismic Coulomb stress changes in the models NP4/5 and TP4/5, in which the lower crust has a higher viscosity than the lithospheric mantle ($\eta_{lc} = 10^{21}$ or 10^{22} Pa s; $\eta_{lm} = 10^{19}$ Pa s), show a large stress triggering zone in the central part of the fault array, i.e. on the source fault, the upper part of RF5, the lower parts of RF7 and 8 and in the parts of RF2 and 10 that are located close to the source fault (Figs. 3c, 4c; Figs. S1b, S2b). In these areas, the stress increases reach maximum values between 0.03 and

0.21 MPa. Stress shadow zones are found in both models in the lower part of RF5 (normal fault: -0.03 MPa; thrust fault: -0.09 MPa) and in the upper parts of RF3, 8 and 11. Receiver fault RF7 shows solely positive stress changes in the normal fault model, whereas its upper part is located in a stress shadow zone in the thrust fault model. Another difference between the two fault models is the location of the stress triggering zone on RF4, which occurs in the upper part of the normal fault but in the lower part of the thrust fault. In contrast, RF1 and 9 show stress triggering zones in their parts that are located close to RF4 in both types of models.

Finally, the results from the models with a lower crustal viscosity of 10^{22} Pa s and a lithospheric mantle viscosity of 10^{21} Pa s (NP6, TP6) show that all faults of the array including the source fault experience an almost

homogeneous distribution of positive Coulomb stress changes on the order of 0.02 MPa (Figs. S1c, S2c). No stress shadow zones occur in these models.

Postseismic Coulomb stress changes in the 10th and 20th years after the earthquake

Depending on the viscosity structure of the lithosphere, the pattern and magnitude of the postseismic Coulomb stress changes show a different evolution through time. In the models NP1 and TP1 ($\eta_{lc} = 10^{20}$ Pa s; $\eta_{lm} = 10^{23}$ Pa s), neither the distribution nor the magnitudes of the stress changes are considerably altered until the 10th and 20th years after the earthquake (Figs. 5a, 6a). Similarly, the positive stress changes remain constant at a value of ~ 0.02 MPa in the models NP6 and TP6 (Online Resource Figs. S3c, S4c). In contrast, the models involving lower viscosities either of the lower crust or the lithospheric mantle exhibit considerable changes in the distribution and magnitudes of the Coulomb stress changes. Models with a viscosity of $\eta_{lc} = 10^{18}$ Pa s (NP2/3, TP2/3) show similar evolutions, regardless of the viscosity of the lithospheric mantle (cf., Figs. 5b, 6b with Figs. S3a and S4a). In these models, most stress shadow zones of the 1st year have shifted their position on the fault plane (e.g. RF1, 9) or turned into stress triggering zones in the 10th year (e.g. RF2, 10). On some faults, the distribution of positive and negative stress changes in the 10th year is inverse to the 1st year (e.g. normal RF7, thrust fault RF4). One of the faults, on which the stress change pattern remained almost constant, is RF8, which still shows a stress shadow zone in its upper part. This stress shadow zone disappears until the 20th year in the normal fault model (Fig. 5b); in the thrust fault, the area becomes smaller (Fig. 6b). In contrast, the zone of negative stress changes that was present during the 1st year in the lower part of normal fault RF5 has disappeared. In the thrust fault model, the source fault experiences a stress decrease in its lower half, which is not observed in the normal fault model. Generally, the magnitude of the stress change on the faults has dropped by an order of magnitude (Figs. 3b, 4b, 5b, 6b). For example, the maximum of the stress increase on fault RF5 dropped from 0.55 to 0.07 MPa in the normal fault model and from 2.19 to 0.12 MPa in the thrust fault model. The highest positive stress changes in the 10th year on receiver faults occur on normal fault RF7 (0.09 MPa) and thrust fault RF5 (0.12 MPa). The largest stress decrease is observed on normal fault RF4 (-0.07 MPa) and on thrust fault RF7 (-0.05 MPa).

Models with a low viscosity of the lithospheric mantle (NP4/5, TP4/5) show an almost identical evolution for the two different viscosities of the lower crust (Figs. 5c, 6c, S1b, S2b). In these models, the overall spatial distribution of stress triggering and shadow zones has remained almost

the same between the 1st and 10th year, but the stress shadow zones have become smaller or disappeared. There are no new stress shadow zones. This trend is also observed in the 20th year (e.g. RF4). Compared to the models with a low viscosity of the lower crust, the difference between the magnitudes of the stress changes in the 1st and 10th year is smaller. For example, the value of the stress decrease on both normal and thrust fault RF4 changed from about -0.05 MPa in the 1st year to -0.02 MPa in the 10th year. The highest stress increase on the receiver faults during the 10th year occurs near the surface at the tips of RF2 and 10 (0.07 MPa) in the normal fault model and on RF5 (0.10 MPa) in the thrust fault model.

To further illustrate the temporal evolution of the Coulomb stress changes, Fig. 7 shows profiles of the Coulomb stress changes in down-dip direction along receiver faults RF5 and 7, while Fig. 8 depicts how the Coulomb stress evolves over a time period of 100 a after the earthquake at the centres of RF5 and 7. The profiles derived from models NP1/TP1 show that the amplitude of the Coulomb stress changes and also the crossings with the zero line do not experience major changes between the 1st, 10th and 20th year after the earthquake (Fig. 7). In contrast, the stress changes differ by an order of magnitude between the 1st year and the 10th/20th years (see insets) in models NP3/TP3. Also, the transitions between negative and positive stress changes and vice versa change their number and locations through time. For example, RF 5 shows two areas with negative stress changes in the 1st year but later only one large area in the fault centre (cf., Figs. 4, 6). Profiles from models NP5/TP5 show a decrease in stress change amplitudes over time. In the normal fault model, RF5 experiences a temporal change from negative to positive stress changes in its lower part between the 10th and 20th year.

The postseismic stress evolution at the centre of RF5 and 7 through time is shown in Fig. 8. The left panel shows the total Coulomb stress, whereas the right panel shows the stress changes induced by viscoelastic relaxation only. For low viscosities of the lower crust (NP3/TP3) and lithospheric mantle (NP5/TP5), the evolution of the Coulomb stress during first 10–30 years is dominated by the signal from viscoelastic relaxation. Afterwards, the transient signal diminishes. In models NP1/TP1, the stress changes arising from viscoelastic relaxation are less pronounced but recognizable over a longer time period compared to models with lower viscosities. In models NP3 and TP3, RF5 experiences a different stress evolution. As normal fault, RF5 first shows a stress increase before a ~ 10 -a-long phase of almost constant stress, which results from the stress decrease caused by viscoelastic flow. As a thrust fault, RF5 shows a strong stress decrease in the early postseismic phase due to viscoelastic relaxation before the interseismic signal prevails after ~ 40 years after the earthquake.

Discussion

Our three-dimensional finite-element models show that the postseismic Coulomb stress changes due to viscoelastic relaxation play an important role for the stress evolution on fault planes and hence the seismic hazard of a region. In our models, the maximum postseismic stress increase on the receiver faults has a value of up to 2.5 MPa/a, which would be sufficient to trigger another earthquake. Viscoelastic relaxation modifies the static stress changes in a way that the Coulomb stress changes on the receiver faults vary significantly through space and time. Depending on the viscosity of the lithospheric layers and the position of the receiver faults relative to the source fault, static stress shadow zones can, over time, turn into postseismic stress triggering zones and vice versa. The temporal evolution of the postseismic relaxation and stress changes is primarily controlled by the layer with the lowest viscosity (Figs. 3, 4, 5, 6). Our results show that the existence of a layer with low viscosity leads to high values of Coulomb stress changes, even if the other layer has a high viscosity. The total postseismic Coulomb stress changes are a superposition of the stress changes caused by viscoelastic relaxation and the interseismic stress increase (Fig. 8). Viscoelastic relaxation can lead to positive or negative stress changes, whereas the interseismic strain accumulation is associated only with a stress increase. Postseismic relaxation of the viscoelastic layers can therefore influence the loading of the fault in the elastic upper crust during the postseismic phase (e.g. Hearn et al. 2002; Kenner 2004; Ellis et al. 2006; DiCaprio et al. 2007). Furthermore, the stress changes caused by viscoelastic relaxation vary in space and time (especially for low viscosities), whereas the interseismic stress increase is approximately constant (0.01–0.02 MPa in our models). The relative contribution of viscoelastic relaxation and interseismic strain accumulation to the total postseismic stress change depends on the viscosity of the lithosphere. For viscosities of $\sim 10^{20}$ Pa s or less and the extension/shortening rates used in our models, transient stress changes due to viscoelastic relaxation outweigh the continuous stress increase due to interseismic strain accumulation for up to several decades, resulting in higher positive Coulomb stress changes or net negative stress changes on the individual receiver fault (Figs. 3, 4, 5, 6, 7, 8).

In the following, we discuss the differences between the coseismic and postseismic Coulomb stress changes and the differences between the normal and thrust fault models (Sect. “Differences between coseismic and postseismic Coulomb stress changes on normal and thrust faults”). Also, we evaluate the influence of stress changes arising from viscoelastic relaxation and stress changes caused by the ongoing extension or shortening as well as the temporal evolution of stress changes and the influence of viscosity.

In a second and third step, we link the Coulomb stress changes to the postseismic movements in the crust and lithospheric mantle to explain the obtained stress change distributions (Sect. “Causes of the postseismic Coulomb stress changes”) and compare our results with previous studies and examples from nature (Sect. “Comparison with Coulomb stress patterns after natural earthquakes”).

Differences between coseismic and postseismic Coulomb stress changes on normal and thrust faults

As our model results show, considerable differences exist in the distribution of coseismic and postseismic stress changes. Whereas the coseismic stress changes are almost independent of the viscosity, the postseismic stress changes strongly depend on this parameter. In the coseismic phase, receiver faults in the along-strike direction of the source fault generally show a stress increase, while most receiver faults parallel to the source fault are dominated by negative stress changes (Fig. 2). In the postseismic phase, however, larger zones of positive stress changes develop on the receiver faults parallel to the source fault (Figs. 3, 4; Online Resource Figs. S1, S2). Faults 2 and 10 generally show positive stress changes during both the coseismic and postseismic phase. On several other receiver faults, the distribution of postseismic stress triggering and shadow zones is inverse to the coseismic distribution. This is particularly pronounced in the models TP2 and TP3, e.g. where the upper part of faults RF3 and 11 undergo a coseismic stress decrease and a postseismic stress increase. Apart from the spatial pattern, coseismic and postseismic phases also differ with respect to the magnitude of the stress changes. Static stress changes on the receiver faults are in the range of -12.0 MPa (thrust RF5) to $+5.0$ MPa (normal RF5). Postseismic stress changes are generally smaller and strongly depend on the viscosity and on the time elapsed after the earthquake. For low viscosities, postseismic stress changes on receiver faults can reach maximum values of -3.0 MPa/a (NP2/3, RF5) and $+2.2$ MPa/a (TP2/3, RF5) in the 1st year.

Our models reveal that normal and thrust faults show remarkable differences in the postseismic stress change evolution (cf., Figs. 5, 6), which can be mainly attributed to difference in fault dip. As shown by Bagge and Hampel (2016) for coseismic stress changes, a change in fault dip and hence the fault plane size leads to differences in the distribution of stress shadow and triggering zones on normal and thrust faults. In the postseismic phase, the differences between normal and thrust faults become even more pronounced because the steeper dip of normal faults compared to thrust faults causes different coseismic loading of the viscoelastic layers. As a consequence, the postseismic movements in the viscoelastic layers and hence the

postseismic Coulomb stress changes are not the same on normal and thrust faults (Fig. 9; see Sect. “Causes of the postseismic Coulomb stress changes” for details). Furthermore, the normal and thrust faults develop under different orientations of the principal stresses, which also leads to differences in postseismic relaxation patterns (e.g. Hampel and Hetzel 2015). With respect to the magnitude of the postseismic Coulomb stress changes, normal and thrust fault models with the same viscosity structure show the same order of magnitude, although the position of the highest stress changes may differ between the fault types.

Causes of the postseismic Coulomb stress changes

The distribution and spatiotemporal evolution of the postseismic Coulomb stress changes are ultimately caused by the postseismic movements in the lithosphere. Generally, the coseismic fault slip and the induced flow in the viscoelastic lithospheric layers perturb the velocity field induced by the far-field deformation, with the consequence that the postseismic velocities both at depth and at the surface show a complex spatiotemporal evolution (Fig. 9). Peak velocities associated with viscoelastic flow generally occur in a broad zone below the source fault near the boundary between the upper and lower crust (Fig. 9a–d) or near the boundary between lower crust and lithospheric mantle (Fig. 9e, f). The differential movements in viscoelastic layers are also responsible for the movements at the surface of the model although the resulting surface velocity field does not necessarily reflect the actual velocity pattern at depth regarding magnitude and direction of movement (e.g. Fig. 9c, d). In accordance with earlier studies on strike-slip faults (Hearn 2003) and dip-slip faults (Hampel and Hetzel 2015), the magnitude of the surface velocities is sufficiently large to be detected by GPS measurements, while the surface velocity pattern generally agrees with observation from natural events like the 1999 Izmit earthquake (Ergintav et al. 2002) and the 2009 L’Aquila earthquake (Serpelloni et al. 2012).

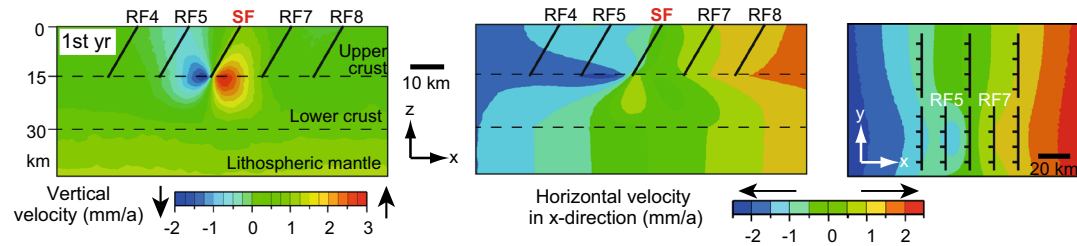
The spatial distribution of these postseismic velocities results in different domains of extension and shortening in both normal and thrust fault models (cf., Hampel and Hetzel 2015), which develop within the lithosphere and at the surface. These domains of extension and shortening are the ones that control the distribution and sign of the Coulomb stress changes on the receiver faults (compare Figs. 3, 4 with Fig. 9). Generally, a receiver normal fault located in a domain of enhanced horizontal extension experiences positive stress changes that exceed the interseismic stress increases; a normal fault located in a domain of shortening exhibits negative stress changes. The opposite holds for receiver thrust faults. As the postseismic velocities and hence the domains of extension and shortening change in

time and space due to the ongoing viscoelastic relaxation, the magnitude and spatial pattern of the Coulomb stress changes also evolves through time. In the models NP1/TP1, the postseismic movements change only negligibly between the 1st (Fig. 9a, b) and the 10th and 20th year (not shown in figure). As a result, the distribution and magnitude of the Coulomb stress changes do also not change significantly (see Figs. 5a, 6a and profiles in left panel of Fig. 7). For example, receiver fault RF 7 experiences high positive stress changes because of enhanced extension (normal fault model) and shortening (thrust fault model). Around normal fault RF 5, the postseismic surface velocity field in the normal fault model indicates an area of horizontal shortening in the source fault hanging wall (Fig. 9a, right panel), which leads to negative Coulomb stress changes on the upper part of receiver fault RF 5 (Fig. 3a). For a low viscosity of the lower crust (models NP3/TP3), the postseismic velocities decrease by an order of magnitude between the 1st and 10th year (Fig. 9c, d). The surface velocity field is highly disturbed, which results in alternating areas of extension and shortening in both normal and thrust fault models (cf., Hampel and Hetzel 2015). The shift of locations with peak velocities through time and the inversion of movement directions between the 1st and 10th year after the earthquake (Fig. 9c) explains the corresponding sign reversals in the Coulomb stress changes, for example on RF 4 (Fig. 5b). Between the 10th and 20th year, the postseismic velocities decrease without major changes in their spatial pattern, which explains the decrease in magnitude of the Coulomb stress changes. Their principal pattern remains almost unaltered except for the fact that the areas with negative stress changes become smaller or disappear (Figs. 5b, 6b) due to the interseismic stress increase. In models NP5/TP5, in which the lithospheric mantle has a lower viscosity than the lower crust, the vertical velocity field shows an almost circular area of uplift (normal fault model) and subsidence (thrust fault model) below the source fault (Fig. 9e, f). These vertical movements combine with the horizontal movements such that the source fault itself and especially receiver faults RF 7 and RF 2 are brought closer to failure in both models (Figs. 5c, 6c). In contrast to models NP3/TP3, the peak velocities decrease through time without major shifts in their location (Fig. 9e, f), which explains why the stress changes due to viscoelastic relaxation decrease without major changes in their distribution except for the disappearance of negative stress changes (Figs. 5c, 6c).

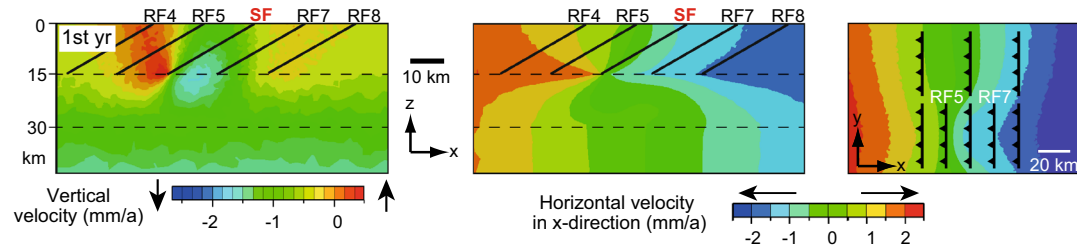
Comparison with Coulomb stress patterns after natural earthquakes

The generalized set-up of models offers the opportunity to compare the principal patterns derived from our models

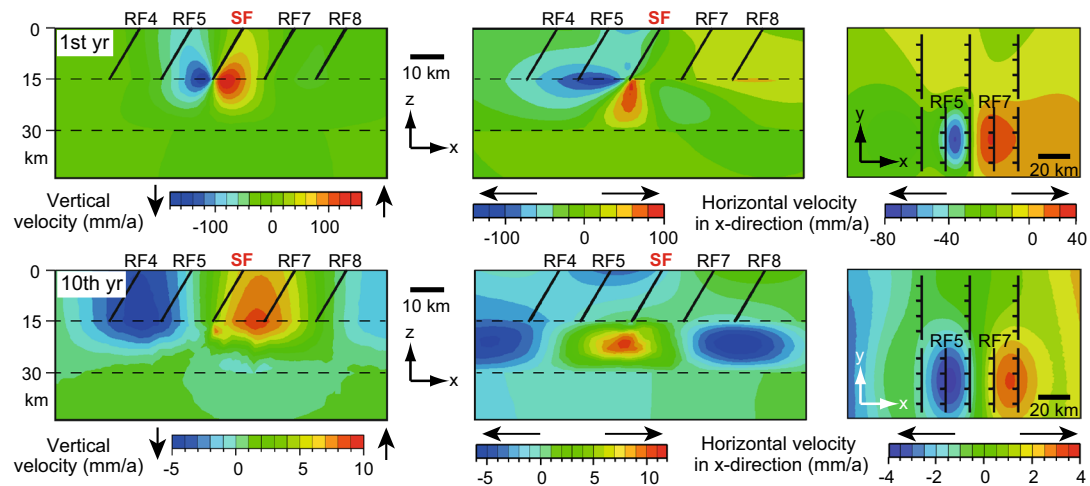
a Model NP1 ($\eta_{lc} = 10^{20}$ Pa s; $\eta_{lm} = 10^{23}$ Pa s)



b Model TP1 ($\eta_{lc} = 10^{20}$ Pa s; $\eta_{lm} = 10^{23}$ Pa s)



c Model NP3 ($\eta_{lc} = 10^{18}$ Pa s; $\eta_{lm} = 10^{23}$ Pa s)



d Model TP3 ($\eta_{lc} = 10^{18}$ Pa s; $\eta_{lm} = 10^{23}$ Pa s)

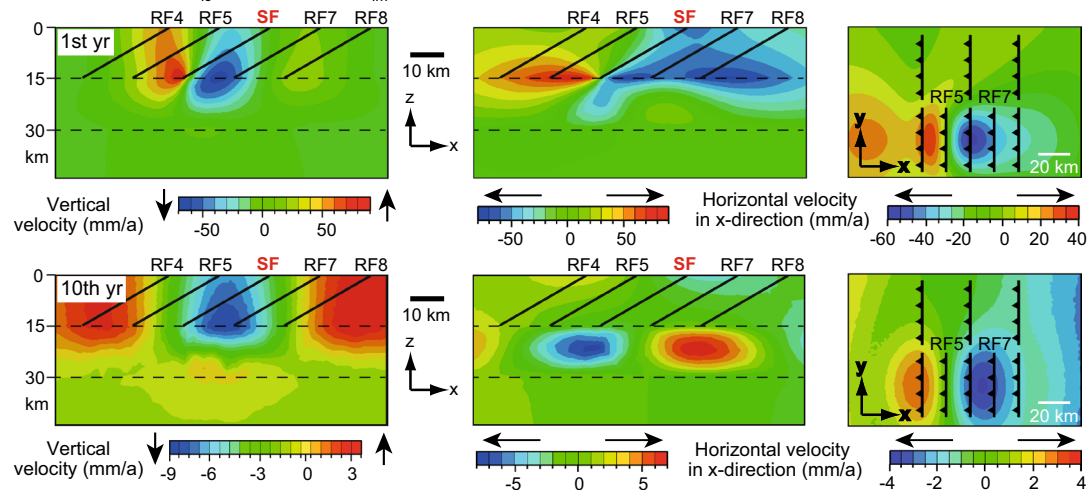


Fig. 9 Postseismic velocity fields derived from the models (a) NP1, (b) TP1, (c) NP3, (d) TP3, (e) NP5 and (f) TP5. Velocities are averaged over a period of 1 year; e.g. the velocity at 10 years after the earthquake is the average over the time interval from 9 to 10 years. All diagrams show the central part of the model, either as cross section (left and central panels) or as map view of the model surface (right panel)

with postseismic Coulomb stress change patterns derived from models for specific natural earthquakes, where postseismic stress changes are influenced by local geological conditions. A prominent example of an earthquake, for which postseismic stress changes have been calculated, is the 2008 $M_w=7.9$ Wenchuan (China) oblique thrust fault earthquake (Chen et al. 2011; Luo and Liu 2010; Nalbant and McCloskey 2011; Wang et al. 2014). This earthquake probably triggered the 2013 $M_w=6.6$ Lushan thrust earthquake, which occurred around 45 km south-west of the 2008 event (Wang et al. 2014). The spatial relation between the faults ruptured by the two earthquakes is comparable to the position of our model receiver fault RF10 relative to the source fault. With respect to the viscosity structure, our model TP4 best matches the model used by Wang et al. (2014). Combining our modelled coseismic Coulomb stress changes (Fig. 2) with the results of model TP4 for the postseismic stress changes (Figs. S2b, S4b), we derive that the fault ruptured by the Lushan earthquake experienced solely positive stress changes during and after the Wenchuan earthquake. For our $M_w \approx 7$ model earthquake, we obtain maximum static stress changes of ~ 3.0 MPa and maximum postseismic stress changes of 0.07 and 0.04 MPa in the 1st and 10th year after the earthquake, respectively. Our results generally agree with the predictions of positive static and postseismic stress changes (Luo and Liu 2010; Nalbant and McCloskey 2011; Parsons et al. 2008; Wang et al. 2014) for this region, although the differences in earthquake magnitude, dip and size of the source fault and assumed lithospheric structure lead to different predictions for the stress change magnitudes. For example, Wang et al. (2014) estimated a stress increase of 0.007 MPa on the fault plane of the Lushan earthquake caused by 5 years of postseismic relaxation of the Wenchuan earthquake. Altogether, our model supports the conclusion that the Lushan earthquake was triggered by the Wenchuan earthquake. For other faults like the Longriba fault that is located in the hanging wall of the Longmenshan fault, Wang et al. (2014) obtain a postseismic stress decrease. They evaluated the postseismic stress changes at a depth of 10 km and argue that only negligible variations occur in the depth range of 5–15 km. In our model TP4, stress shadow zones indeed occur in the lower parts of faults RF4, RF5 and RF9, but these faults also experience considerably high positive stress changes in other parts. This example underlines that it is crucial

to consider the Coulomb stress change distribution on the whole fault plane.

Stress interaction between normal faults caused by viscoelastic relaxation has been investigated by Nostro et al. (2001) by using whole-Earth models with viscoelastic layers. They calculated the postseismic stress changes for the 1980 $M_w=6.9$ Irpinia earthquake (southern Apennines) on a 60° -dipping source fault with a length of 35 km. Results were shown in map view for a depth of 17 km and a time point 100 a after the earthquake and as time-stress plots for a fixed point and a time interval of 1000 a after the earthquake. Similar to our models, the viscoelastic models by Nostro et al. (2001) show postseismic stress triggering zones in the along-strike direction of the source fault and alternating stress shadow and triggering zones in the hanging wall and footwall of the source fault. Based on a parameter study, in which Nostro et al. (2001) analysed the temporal evolution of the postseismic relaxation and the influence of the layer thickness and viscosity, but without considering background deformation, they concluded that the shallowest viscoelastic layer dominates the postseismic Coulomb stress changes. Our results additionally show that the layer with the lowest viscosity has the largest influence on the postseismic stress changes.

Conclusions

Three-dimensional finite-element modelling of the postseismic viscous flow in the lower crust and lithospheric mantle enables evaluating the spatiotemporal evolution of transient stress changes on intra-continental dip-slip faults and their dependence on the viscosity of the lithospheric layers. As experiments with different viscosity structures of the lithosphere show, the layer of the lowest viscosity has the strongest influence on postseismic Coulomb stress change patterns. Postseismic stress changes can modify static stress changes in a way that coseismic stress triggering zones can change to postseismic stress shadow zones and *vice versa*. On the other hand, the magnitude of both positive and negative coseismic stress changes can increase during the postseismic phase, implying that earthquakes on receiver faults can be additionally promoted or delayed. Our results also underline the importance of considering the combined effect of stress changes caused by the ongoing extension or shortening (leading to an interseismic stress increase) and by the postseismic relaxation (leading to stress increase or decrease). The relative contribution of postseismic relaxation and interseismic strain accumulation to the stress state on the receiver faults depends, among other factors like the regional deformation rate and the

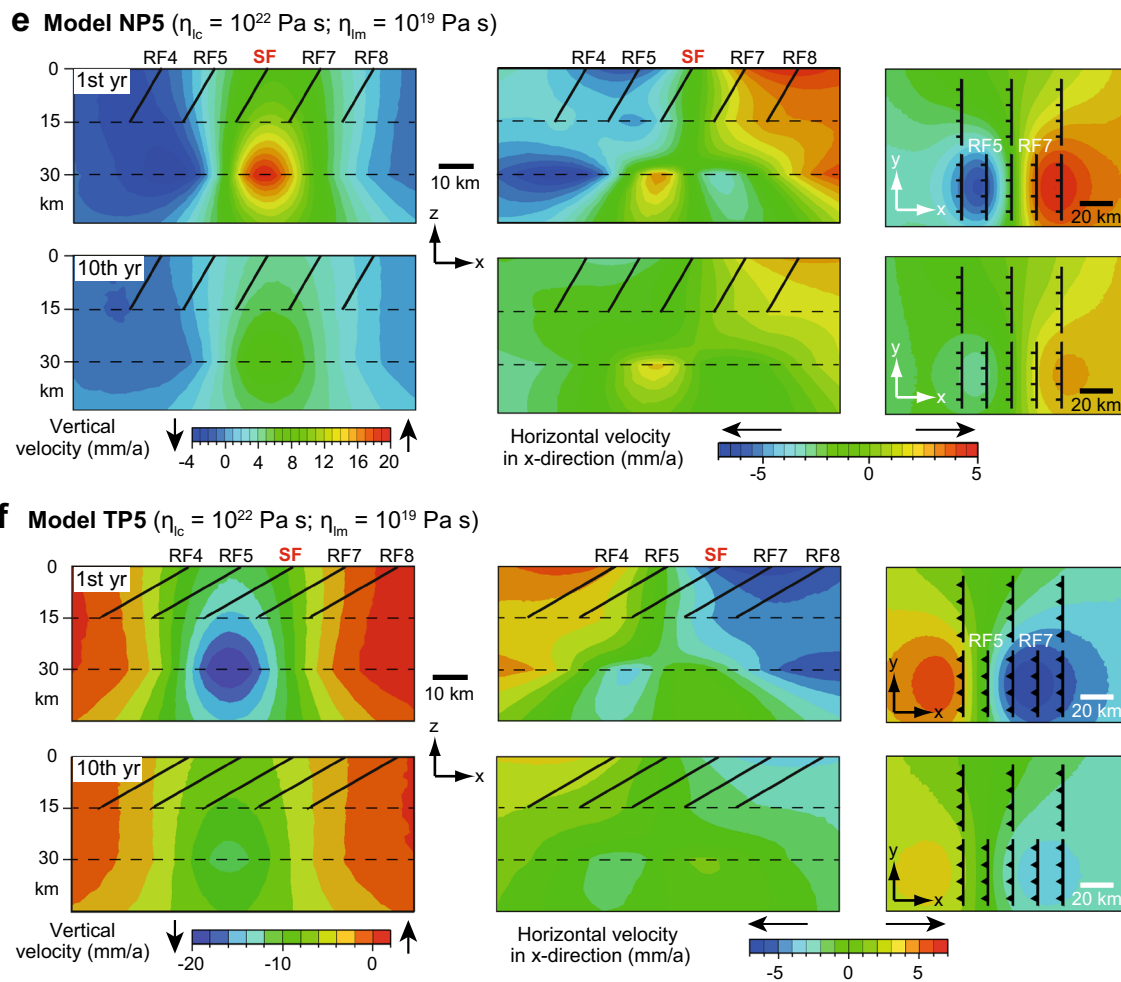


Fig. 9 (continued)

magnitude of the earthquake, on the location of the receiver fault relative to the source fault, the time elapsed after the earthquake, the fault dip and the viscosity.

Acknowledgements We thank the topic editor J. Nüchter and three anonymous reviewers for their constructive comments, which greatly improved the manuscript. We used the Generic Mapping Tools by Wessel and Smith (1998) for creating some of the figures.

References

- Amelung F, Bell JW (2003) Interferometric synthetic aperture radar observations of the 1994 Double Spring Flat, Nevada, earthquake (M5.9): main shock accompanied by triggered slip on a conjugate fault. *J Geophys Res* 108:2433. doi:[10.1029/2002JB001953](https://doi.org/10.1029/2002JB001953)
- Bagge M, Hampel A (2016) Three-dimensional finite-element modelling of coseismic Coulomb stress changes on intra-continental dip-slip faults. *Tectonophysics* 684:52–62. doi:[10.1016/j.tecto.2015.10.006](https://doi.org/10.1016/j.tecto.2015.10.006)
- Belardinelli ME, Cocco M, Coutant O, Cotton F (1999) Redistribution of dynamic stress during coseismic ruptures: evidence for fault interaction and earthquake triggering. *J Geophys Res* 104:14925–14945. doi:[10.1029/1999JB900094](https://doi.org/10.1029/1999JB900094)
- Bills BG, Currey DR, Marshall GA (1994) Viscosity estimates for the crust and upper mantle from patterns of lacustrine shoreline deformation in the Eastern Great Basin. *J Geophys Res* 99:22059–22086
- Bürgmann R, Dresen G (2008) Rheology of the lower crust and upper mantle: evidence from rock mechanics, geodesy, and field observations. *Annu Rev Earth Planet Sci* 36:531–567. doi:[10.1146/annurev.earth.36.031207.124326](https://doi.org/10.1146/annurev.earth.36.031207.124326)
- Burov EB, Watts AB (2006) The long-term strength of the continental lithosphere: “jelly sandwich” or “crème brûlée”? *GSA Today* 16:4–10. doi:[10.1130/1052-5173\(2006\)016<4:tltSOc>2.0.cO;2](https://doi.org/10.1130/1052-5173(2006)016<4:tltSOc>2.0.cO;2)
- Chen WP, Molnar P (1983) Focal depths of intracontinental and intraplate earthquakes and their implications for the thermal and mechanical properties of the lithosphere. *J Geophys Res* 88:4183–4214. doi:[10.1029/JB088iB05p04183](https://doi.org/10.1029/JB088iB05p04183)
- Chen Z, Lin B, Bai W, Cheng X, Wang Y (2011) A study on the influence of the 2008 Wenchuan earthquake on the stability of

- the Qinghai–tibet plateau tectonic block system. *Tectonophysics* 510:94–103. doi:[10.1016/j.tecto.2011.06.020](https://doi.org/10.1016/j.tecto.2011.06.020)
- Cocco M, Rice JR (2002) Pore pressure and poroelasticity effects in Coulomb stress analysis of earthquake interactions. *J Geophys Res* 107:2030. doi:[10.1029/2000JB000138](https://doi.org/10.1029/2000JB000138)
- Diao F, Xiong X, Wang R, Zheng Y, Walter TR, Weng H, Li J (2014) Overlapping post-seismic deformation processes: afterslip and viscoelastic relaxation following the 2011 Mw 9.0 Tohoku (Japan) earthquake. *Geophys J Int* 196:218–229. doi:[10.1093/gji/ggt376](https://doi.org/10.1093/gji/ggt376)
- DiCaprio CJ, Simons M, Kenner SJ, Williams CA (2007) Post-seismic reloading and temporal clustering on a single fault. *Geophys J Int* 172:581–592. doi:[10.1111/j.1365-246X.2007.03622.x](https://doi.org/10.1111/j.1365-246X.2007.03622.x)
- Ellis S, Stöckhert B (2004) Elevated stresses and creep rates beneath the brittle-ductile transition caused by seismic faulting in the upper crust. *J Geophys Res* 109:B05407. doi:[10.1029/2003JB002744](https://doi.org/10.1029/2003JB002744)
- Ellis S, Beavan J, Eberhart-Phillips D, Stöckhert B (2006) Simplified models of the Alpine Fault seismic cycle: stress transfer in the mid-crust. *Geophys J Int* 166:386–402. doi:[10.1111/j.1365-246X.2006.02917.x](https://doi.org/10.1111/j.1365-246X.2006.02917.x)
- Ergintav S, Bürgmann R, McClusky S, Cakmak R, Reilinger RE, Lenk O, Barka A, Gurkan O (2002) Postseismic deformation near the Izmit earthquake 17 August, 1999. *Bull Seism Soc Am* 92:194–207
- Freed AM (2005) Earthquake triggering by static, dynamic, and post-seismic stress transfer. *Annu Rev Earth Planet Sci* 33:335–367. doi:[10.1146/annurev.earth.33.092203.122505](https://doi.org/10.1146/annurev.earth.33.092203.122505)
- Freed AM, Bürgmann R (2004) Evidence of power-law flow in the Mojave desert mantle. *Nature* 430:548–551. doi:[10.1038/nature02784](https://doi.org/10.1038/nature02784)
- Freed AM, Lin J (1998) Time-dependent changes in failure stress following thrust earthquakes. *J Geophys Res* 103:24393–24409. doi:[10.1029/98JB01764](https://doi.org/10.1029/98JB01764)
- Freed AM, Lin J (2001) Delayed triggering of the 1999 Hector Mine earthquake by viscoelastic stress transfer. *Nature* 411:180–183. doi:[10.1038/35075548](https://doi.org/10.1038/35075548)
- Gourmelen N, Amelung F (2005) Postseismic mantle relaxation in the central Nevada seismic belt. *Science* 310:1473–1476. doi:[10.1126/science.1119798](https://doi.org/10.1126/science.1119798)
- Haller KM, Machette MN, Dart RL, Rhea BS (2004) U.S. Quaternary fault and fold database released. *EOS* 85,22:218. doi:[10.1029/2004EO220004](https://doi.org/10.1029/2004EO220004)
- Hampel A, Hetzel R (2012) Temporal variation in fault friction and its effects on the slip evolution of a thrust fault over several earthquake cycles. *Terra Nova* 24:357–362. doi:[10.1111/j.1365-3121.2012.01073.x](https://doi.org/10.1111/j.1365-3121.2012.01073.x)
- Hampel A, Hetzel R (2015) Horizontal surface velocity and strain patterns near thrust and normal faults during the earthquake cycle: the importance of viscoelastic relaxation in the lower crust and implications for interpreting geodetic data. *Tectonics* 34:731–752. doi:[10.1002/2014TC003605](https://doi.org/10.1002/2014TC003605)
- Hampel A, Li T, Maniatis G (2013) Contrasting strike-slip motions on thrust and normal faults: Implications for space-geodetic monitoring of surface deformation. *Geology* 41:299–302. doi:[10.1130/G33927.1](https://doi.org/10.1130/G33927.1)
- Hearn EH (2003) What can GPS data tell us about the dynamics of post-seismic deformation? *Geophys J Int* 155:753–777
- Hearn EH, Bürgmann R, Reilinger R (2002) Dynamics of Izmit earthquake postseismic deformation and loading of the Düzce earthquake hypocenter. *Bull Seismol Soc Am* 92:172–193
- Hetzel R, Tao M, Niedermann S, Strecker MR, Ivy-Ochs S, Kubik PW, Gao B (2004) Implications of the fault scaling law for the growth of topography: mountain ranges in the broken foreland of north-east Tibet. *Terra Nova* 16:157–162. doi:[10.1029/2004EO220004](https://doi.org/10.1029/2004EO220004)
- Jackson J (2002) Strength of the continental lithosphere: time to abandon the jelly sandwich? *GSA Today* 12:4–9
- Kaufmann G, Amelung F (2000) Reservoir-induced deformation and continental rheology in vicinity of Lake Mead, Nevada. *J Geophys Res* 105:16341–16358. doi:[10.1029/2000JB900079](https://doi.org/10.1029/2000JB900079)
- Kenner SJ (2004) Rheological controls on fault loading rates in northern California following the 1906 San Francisco earthquake. *Geophys Res Lett* 31:L01606. doi:[10.1029/2003GL018903](https://doi.org/10.1029/2003GL018903)
- King GC, Stein RS, Lin J (1994) Static Stress changes and the triggering of earthquakes. *Bull Seismol Soc Am* 84:935–953
- Klemperer SL (2006) Crustal flow in Tibet: geophysical evidence for the physical state of Tibetan lithosphere, and inferred patterns of active flow. In: Law R, Searle MP, Godin L (eds.) Channel flow, ductile extrusion and exhumation in continental collision zones. *Geol Soc London Spec Publ* 268:39–70. doi:[10.1144/GSL.SP.2006.268.01.03](https://doi.org/10.1144/GSL.SP.2006.268.01.03)
- Lambert V, Barbot S (2016) Contribution of viscoelastic flow in earthquake cycles within the lithosphere-asthenosphere system. *Geophys Res Lett* 43:10,142–10,154. doi:[10.1002/2016GL070345](https://doi.org/10.1002/2016GL070345)
- Lin J, Stein RS (2004) Stress interaction in thrust and subduction earthquakes and stress interaction between the southern San Andreas and nearby thrust and strike-slip faults. *J Geophys Res* 109:B02303. doi:[10.1029/2003JB002607](https://doi.org/10.1029/2003JB002607)
- Lin J, Stein RS, Meghraoui M, Toda S, Ayadi A, Dorbath C, Belabbes S (2011) Stress transfer among en echelon and opposing thrusts and tear faults: triggering caused by the 2003 $M_w = 6.9$ Zemmouri, Algeria, earthquake. *J Geophys Res* 116:B03305. doi:[10.1029/2010JB007654](https://doi.org/10.1029/2010JB007654)
- Luo G, Liu M (2010) Stress evolution and fault interactions before and after the 2008 Great Wenchuan earthquake. *Tectonophysics* 491:127–140. doi:[10.1016/j.tecto.2009.12.019](https://doi.org/10.1016/j.tecto.2009.12.019)
- Masterlark T, Wang HF (2002) Transient Stress-Coupling Between the 1992 Landers and 1999 Hector Mine, California, Earthquakes. *Bull Seismol Soc Am* 92:1470–1486
- Meyer B, Taponnier P, Bourjot L, Métiévier F, Gaudemer Y, Peltzer G, Guo S, Chen Z (1998) Crustal thickening in Gansu-Qinghai, lithospheric mantle subduction, and oblique, strike-slip controlled growth of the Tibetan Plateau. *Geophys J Int* 135:1–47. doi:[10.1046/j.1365-246X.1998.00567.x](https://doi.org/10.1046/j.1365-246X.1998.00567.x)
- Miller SA, Collettini C, Chiaraluce L, Cocco M, Barchi M, Kaus BJ (2004) Aftershocks driven by a high-pressure CO₂ source at depth. *Nature* 427:724–727. doi:[10.1038/nature02251](https://doi.org/10.1038/nature02251)
- Nalbant SS, McCloskey J (2011) Stress evolution before and after the 2008 Wenchuan, China earthquake. *Earth Planet Sci Lett* 307:222–232. doi:[10.1016/j.epsl.2011.04.039](https://doi.org/10.1016/j.epsl.2011.04.039)
- Nishimura T, Thatcher W (2003) Rheology of the lithosphere inferred from postseismic uplift following the 1959 Hebgen Lake earthquake. *J Geophys Res* 108:2389. doi:[10.1029/2002JB002191](https://doi.org/10.1029/2002JB002191)
- Nostro C, Cocco M, Belardinelli ME (1997) Static stress changes in extensional regimes: an application to Southern Apennines (Italy). *Bull Seismol Soc Am* 87:234–248
- Nostro C, Piersanti A, Cocco M (2001) Normal fault interaction caused by coseismic and postseismic stress changes. *J Geophys Res* 106:19391–19410. doi:[10.1029/2001JB000426](https://doi.org/10.1029/2001JB000426)
- Nüchter J-A, Ellis S (2010) Complex states of stress during the normal faulting seismic cycle: Role of midcrustal postseismic creep. *J Geophys Res* 115:B12. doi:[10.1029/2010JB007557](https://doi.org/10.1029/2010JB007557)
- Nüchter J-A, Ellis S (2011) Mid-crustal controls on episodic stress-field rotation around major reverse, normal and strike-slip faults. *Geol Soc London Spec Publ* 359:187–201. doi:[10.1144/SP359.11](https://doi.org/10.1144/SP359.11)
- Nur A, Mavko G (1974) Postseismic viscoelastic rebound. *Science* 183:204–206

- Okada Y (1992) Internal deformation due to shear and tensile faults in a half-space. *Bull Seismol Soc Am* 82:1018–1040
- Parsons T, Ji C, Kirby E (2008) Stress changes from the 2008 Wenchuan earthquake and increased hazard in the Sichuan basin. *Nature* 454:509–510. doi:[10.1038/nature07177](https://doi.org/10.1038/nature07177)
- Piombo A, Martinelli G, Dragoni M (2005) Post-seismic fluid flow and Coulomb stress changes in a poroelastic medium. *Geophys J Int* 162:507–515. doi:[10.1111/j.1365-246X.2005.02673.x](https://doi.org/10.1111/j.1365-246X.2005.02673.x)
- Pollitz FF (1997) Gravitational viscoelastic postseismic relaxation on a layered spherical Earth. *J Geophys Res* 102:17921–17941. doi:[10.1029/97JB01277](https://doi.org/10.1029/97JB01277)
- Pollitz FF, Stein RS, Sevilgen V, Bürgmann R (2012) The 11 April 2012 east Indian Ocean earthquake triggered large aftershocks worldwide. *Nature* 490:250–255. doi:[10.1038/nature11504](https://doi.org/10.1038/nature11504)
- Roberts GP, Michetti AM (2004) Spatial and temporal variations in growth rates along active normal fault systems: an example from the Lazio–Abruzzo Apennines, central Italy. *J Struct Geol* 26:339–376. doi:[10.1016/S0191-8141\(03\)00103-2](https://doi.org/10.1016/S0191-8141(03)00103-2)
- Rolandone F, Bürgmann R, Nadeau RM (2004) The evolution of the seismic-aseismic transition during the earthquake cycle: constraints from the time-dependent depth distribution of aftershocks. *Geophys Res Lett* 31:L23610. doi:[10.1029/2004GL02137](https://doi.org/10.1029/2004GL02137)
- Ryder I, Bürgmann R, Fielding E (2012) Static stress interactions in extensional earthquake sequences: an example from the South Lunggar Rift, Tibet. *J Geophys Res* 117:B09405. doi:[10.1029/2012JB009365](https://doi.org/10.1029/2012JB009365)
- Ryder I, Wang H, Bie L, Rietbrock A (2014) Geodetic imaging of late postseismic lower crustal flow in Tibet. *Earth Planet Sci Lett* 404:136–143. doi:[10.1016/j.epsl.2014.07.026](https://doi.org/10.1016/j.epsl.2014.07.026)
- Serpelloni E, Anderlini L, Belardinelli ME (2012) Fault geometry, coseismic-slip distribution and Coulomb stress change associated with the 2009 April 6, Mw 6.3, L'Aquila earthquake from inversion of GPS displacements. *Geophys J Int* 188:473–489. doi:[10.1111/j.1365-246X.2011.05279.x](https://doi.org/10.1111/j.1365-246X.2011.05279.x)
- Shi X, Kirby E, Furlong KP, Meng K, Robinson R, Wang E (2015) Crustal strength in central Tibet determined from Holocene shoreline deflection around Siling Co. *Earth Planet Sci Lett* 423:145–154. doi:[10.1016/j.epsl.2015.05.002](https://doi.org/10.1016/j.epsl.2015.05.002)
- Smith BR, Sandwell DT (2006) A model of the earthquake cycle along the San Andreas fault system for the past 1000 years. *J Geophys Res* 111:B101405. doi:[10.1029/2005JB003703](https://doi.org/10.1029/2005JB003703)
- Stein RS (1999) The role of stress transfer in earthquake occurrence. *Nature* 402:605–609
- Stein RS (2003) Earthquake conversations. *Sci Am* 288:72–79. doi:[10.1038/scientificamerican0103-72](https://doi.org/10.1038/scientificamerican0103-72)
- Stein RS, King GC, Lin J (1992) Change in failure stress on the southern san andreas fault system caused by the 1992 magnitude = 7.4 landers earthquake. *Science* 258:1328–1332
- Sun T, Wang K, Iinuma T, Hino R, He J, Fujimoto H, Kido M, Osada Y, Miura S, Ohta Y, Hu Y (2014) Prevalence of viscoelastic relaxation after the 2011 Tohoku-oki earthquake. *Nature* 514:84–87. doi:[10.1038/nature13778](https://doi.org/10.1038/nature13778)
- Wang Y, Wang F, Wang M, Shen ZK, Wan Y (2014) Coulomb stress change and evolution induced by the 2008 Wenchuan earthquake and its delayed triggering of the 2013 M_w 6.6 Lushan earthquake. *Seismol Res Lett* 85:52–59. doi:[10.1785/0220130111](https://doi.org/10.1785/0220130111)
- Wessel P, Smith WH (1998) New, improved version of generic mapping tools released. *Eos Trans Am Geophys Union* 79:579. doi:[10.1029/98EO00426](https://doi.org/10.1029/98EO00426)